Current Pulsation Suppression Method Based on Power Current Closed-Loop Control for a PMSM Under Fluctuating DC-Link Voltage

Jiali Liu and Yongchang Zhang, *Senior Member, IEEE*

***Abstract*—For a single-phase rectifier, a common issue is that there exists a component fluctuating at twice the grid frequency in dc-link voltage due to the fluctuating input power. This fluctuating dc-link voltage causes modulation error, which induces severe phase current pulsation at low frequency. An additional *LC* filter can suppress the voltage fluctuation at the cost of increasing volume and reducing power density. The conventional software method is achieved by the modulation ratio or frequency compensation. However, the compensation methods have limited performance. In this article, a cascaded power current controller is proposed to suppress the current pulsation. The power current is constructed and used as the control target. Accordingly, the power current loop is cascaded between the speed and current loops. Maintaining a constant power current beneficially rejects the current ripple. Compared to the conventional closed-loop method, the proposed method does not need a phase-locked loop or resonant controller. Therefore, it has the ability to suppress current pulsation within a wide frequency range, and can achieve improved dynamic performance due to the fast convergence. Experimental results confirm the expected performance of the proposed method.**

***Index Terms*—Cascaded power current controller, compensation, fluctuating component, phase current pulsation, single-phase rectifier.**

I. Introduction

PERMANENT magnet synchronous machines (PMSMs) have various advantages as motor drives in industrial applications and household electrical appliances [1], [2]. Usually, the motor is fed by an ac–dc–ac power converter, which contains a single-phase rectifier, buffer capacitor, and voltage source inverter [3], [4]. For different applications, there are different rectifiers. Boost-type rectifiers are usually used in home applications, and single-phase PWM rectifiers are used in railway traction drives. However, for single-phase power converters, a common issue is that there exists a component fluctuating at twice the grid frequency in the dc-link voltage. Due to the fluctuating voltage, digital pulsewidth modulation (PWM), and one-step sample, a modulation error appears in the output voltage vector, which induces q-axis current pulsation at twice the grid frequency [5], [6].

To solve the problems of fluctuating component in the phase current, a simple and effective solution is using an *LC* resonant filter to absorb the fluctuating component. The *LC* filter is parallel with the dc-link capacitor, and the resonant frequency is set as twice the grid frequency. However, the resonant frequency is variable when the parameters drift [7]. Supposing that the resonant frequency is constant, the designed parameters are still not suitable when the grid frequency deviates. Moreover, the additional hardware increases the cost, makes the system bulky, and reduces the power density of system. Other hardware solutions include the employment of a larger electrolytic capacitor filter or active filter [8], [9]. The usage of a larger electrolytic capacitor decreases the lifetime of power system since the capacitor is sensitive to the inner temperature. In summary, although the hardware methods are simple and effective, they are sensitive to the parameter drift and grid frequency deviation. Moreover, it brings additional loss and risk of failure.

Compared with hardware solutions, software solutions are of more interest. Many methods have been proposed to suppress the current pulsation [10]–[12]. From the view of control strategy, these methods can be classified into two types: feed-forward methods and closed-loop feedback methods. For feed-forward compensation, the instantaneous dc-link voltage is sampled and used to adjust the modulation index [7], [13], [14]. The modulation error is eliminated by the compensated modulation index, which is negatively related to the fluctuating voltage. Although this method is easy to implement and responds quickly to voltage fluctuation disturbance, the effectiveness is affected by the acquisition accuracy of the instantaneous dc-link voltage. In practical application, it is difficult to measure this voltage accurately. To improve the accuracy of voltage measurement, a repetitive controller and linear observers have been proposed to predict the dc-link voltage [15]–[18]. Different from the modulation index compensation, frequency compensation methods were proposed in [19] and [20]. Based on the model analysis, a compensation value is derived to adjust the output voltage vector [21]. Ultimately, the current pulsation is suppressed by

Manuscript received January 24, 2021; revised May 9, 2021; accepted June 24, 2021. Date of publication June 30, 2021; date of current version September 16, 2021. This work was supported by the National Natural Science Foundation of China under Grant 52077002. Recommended for publication by Associate Editor S. K. Panda. *(Corresponding author: Yongchang Zhang.)*

Jiali Liu is with the Inverter Technologies Engineering Research Center of Beijing, North China University of Technology, Beijing 100144, China (e-mail: 1776334054@qq.com).

Yongchang Zhang is with the School of Electrical and Electronic Engineering, North China Electric Power University, Beijing 102206, China, and also with the Inverter Technologies Engineering Research Center of Beijing, North China University of Technology, Beijing 100144, China (e-mail: yozhang@ieee.org).

Color versions of one or more figures in this article are available at https://doi.org/10.1109/TPEL.2021.3093586.

Digital Object Identifier 10.1109/TPEL.2021.3093586

the compensated frequency, which is derived by the fluctuating voltage. Unfortunately, additional high-order harmonics are produced when the compensated frequency is applied. Lei *et al.* [22] proposed a method that utilizes another compensation component to suppress the introduced harmonics. Unfortunately, the frequency compensation is effective only for induction motors, not suitable for a PMSM [11]. These methods are effective when the fluctuation in the dc-link voltage is sinusoidal. However, in practical application, the dc-link voltage may contain other fluctuating components with respect to the fluctuating output power. The effectiveness is limited when the voltage contains different fluctuating components.

For closed-loop feedback methods, the current rather than the dc-link voltage is used as the feedback variable. In [23], the pulsation of instantaneous phase current is obtained to adjust the modulation index. The disadvantage of this method is the complicated calculation of the magnitude of space vector current, and only one feedback loop is used. If the tuning of parameters is not adequate, the compensation value becomes a disturbance for the normal current loop control [24]. In [25], a resonant controller is placed in parallel with the PI controller to eliminate current pulsation in the synchronous frame. Although the resonant controller has a larger gain at twice the grid frequency, the dynamic performance is poor when the current changes abruptly. Lei *et al.* [26] proposed a frequency compensation method that eliminates the ripple of the q-axis current at twice the grid frequency through closed-loop control. An additional control loop is adopted to regulate the q-axis current, which can reduce the torque ripple and current pulsation. However, the convergence time is long, leading to limited dynamic performance due to the usage of a resonant controller and phase-locked loop.

In this article, a power current control method is proposed to suppress the low-frequency fluctuation in phase current. The power current is constructed and used as the control target. Controlling the power current constant beneficially rejects current ripple. Note that the command power current can be set not only a constant value but also a variable fluctuating at the double grid frequency of 100 Hz. This can be used for the application with even smaller capacitor, including electrolytic capacitorless, in which the requirement becomes reducing the harmonics of current in grid. In that case, the control target can still be the constructed power current since it affects directly both the grid current and the motor currents. This method aims to eliminate the q-axis current pulsation and improve the antidisturbance ability for current loops. Different from the conventional compensation method, the additional power current loop is cascaded between the speed loop and current loop. Compared with conventional methods, the performance of the proposed power current control is improved significantly. First, the closed-loop feedback control ensures the insensitivity to the accuracy of measured dc-link voltage. Second, this control method can suppress the current pulsation effectively, even though the pulsation frequency deviates from 100 or 120 Hz. In addition, the pulsation components that contain multiple frequencies can be suppressed simultaneously. Finally, the fast convergence helps improve the dynamic performance. The effectiveness of the proposed method is confirmed by the experimental results.

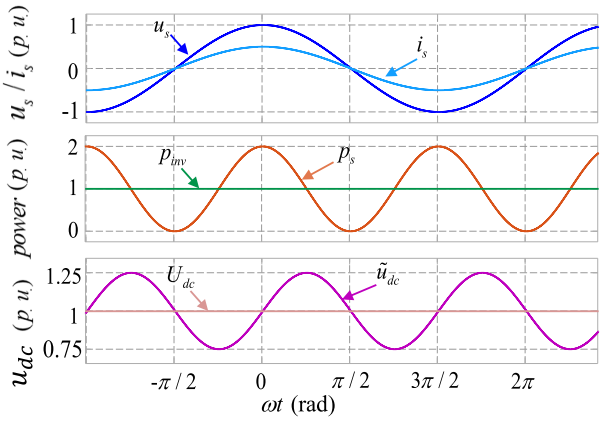

Fig. 1. Input grid voltage, current, power, and dc-link voltage.

II. Mechanism of DC-Link Voltage Fluctuation

The input grid voltage u_s and current i_s are defined as

$$u_s = U_s \cos(\omega_g t) \tag{1}$$

$$i_s = I_s \cos(\omega_g t + \varphi) \tag{2}$$

where U_s is the peak value of u_s, I_s is the peak value of i_s, ω_g is the angular frequency of the input voltage, and φ is the lagging angle between the voltage u_s and the current i_s. Due to the regulation of the active power filter, φ is assumed to be zero. The input instantaneous power is defined as $p_s = u_s * i_s$. Therefore, the input power is presented as follows:

$$p_s = \frac{U_s I_s}{2} + \frac{U_s I_s}{2} \cos(2\omega_g t). \tag{3}$$

From (3), the input power contains a dc component $\frac{U_s I_s}{2}$ and an ac component $\frac{U_s I_s}{2} \cos(2\omega_g t)$. The input current, voltage, and power are depicted in Fig. 1.

For a power converter, the input power is distributed to the dc-link capacitor and inverter. Usually, the inverter outputs a constant power, and the capacitor absorbs the ac component power of p_s. The power equations are shown as

$$\begin{aligned} p_{\text{inv}} &= u_{\text{dc}} i_{\text{inv}} \\ p_c &= C \cdot u_{\text{dc}} \frac{du_{\text{dc}}}{dt} \\ p_s &= p_{\text{inv}} + p_c \end{aligned} \tag{4}$$

where p_{inv} is the inverter power, p_c is the dc-link capacitor power, i_{inv} is the input inverter current, C is the capacitance, and u_{dc} is the dc-link voltage, which contains a dc component U_{dc} and a ripple component $\widetilde{u}_{\text{dc}}$

$$u_{\text{dc}} = U_{\text{dc}} + \widetilde{u}_{\text{dc}}. \tag{5}$$

According to the principle of power balancing, the following equations can be formulated:

$$\frac{U_s I_s}{2} = u_{\text{dc}} i_{\text{inv}} \tag{6}$$

$$\frac{U_s I_s}{2} \cos(2\omega_g t) = C \cdot u_{\text{dc}} \frac{du_{\text{dc}}}{dt}. \tag{7}$$

Note that (6) and (7) are suitable for steady state only. Since $\widetilde{u}_{\rm dc}$ is smaller than $U_{\rm dc}$, (7) can be simplified as

$$\frac{U_s I_s}{2}\cos(2\omega_g t) = C\cdot U_{\rm dc}\frac{d\widetilde{u}_{\rm dc}}{dt}. \tag{8}$$

From (6) and (8), in steady state, the ripple voltage is deduced as

$$\widetilde{u}_{\rm dc} = \frac{u_{\rm dc} i_{\rm inv}\sin(2\omega_g t)}{2\omega_g C U_{\rm dc}}. \tag{9}$$

The ripple voltage is positively correlated with the inverter power or current and negatively correlated with the capacitance. Note that the inverter power may contain an alternating component when a cyclical fluctuation load is applied

$$p_{\rm inv} = P_{\rm inv} + \widetilde{p}_{\rm inv} \tag{10}$$

$$\widetilde{p}_{\rm inv} = \Delta p\cos(\omega_l t + \phi) \tag{11}$$

where $P_{\rm inv}$ is the average value of inverter power, Δp is the amplitude of ripple power, ω_l is the ripple angular frequency, and ϕ is the initial phase. Ultimately, the expression of ripple voltage can be rewritten as

$$\widetilde{u}_{\rm dc} = \frac{P_{\rm inv}\sin(2\omega_g t)}{2\omega_g C U_{\rm dc}} + \frac{\Delta p\sin(\omega_\Delta t)}{4\omega_\Delta C U_{\rm dc}} + \frac{\Delta p\sin(\omega_\Sigma t)}{4\omega_\Sigma C U_{\rm dc}}. \tag{12}$$

Here, ω_Δ is the difference between $2\omega_g$ and ω_l, and ω_Σ is the sum of $2\omega_g$ and ω_l. The first term of (12) shows the voltage ripple caused by input power and the average output power. The second and third terms show the voltage ripples caused by the output ripple power. Usually, the first term is the dominant component.

III. Influence of DC-Link Voltage Fluctuation

Generally, the fluctuating dc-link voltage causes a current beat phenomenon. Many other factors, such as digital PWM, low switching frequency, and one-sampling-ahead requirement, make the current fluctuate. Additionally, in practical applications, the limited current tracking ability makes the fluctuated current worse. In the range of linear modulation, the modulation index is defined as

$$m = \frac{u_{\rm sref}}{u_{\rm sdc}/\sqrt{3}} \tag{13}$$

where $u_{\rm sdc}$ is the sampled dc-link voltage and $u_{\rm sref}$ is the amplitude of command voltage.

From (9), the former can be expressed as

$$u_{\rm sdc} = U_{\rm dc} + \Delta u_{\rm dc}\sin(2\omega_g t). \tag{14}$$

As shown in Fig. 2, through inverter amplification, the output voltage vector can be expressed as

$$u_{so} = m\cdot u_{\rm sbase}\cdot e^{j\theta_r} \tag{15}$$

where the base voltage is defined as $u_{\rm sbase} = u_{\rm dc}/\sqrt{3}$ and the rotor position is defined as $\theta_r = \omega_r t$. However, due to the phase delay caused by digital PWM and one-step sampling, the real-time voltage becomes

$$u_{\rm dc} = U_{\rm dc} + \Delta u_{\rm dc}\sin(2\omega_g t + \delta) \tag{16}$$

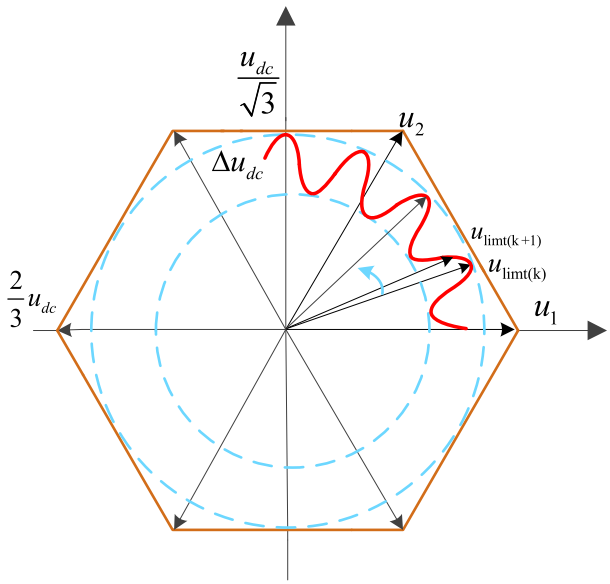

Fig. 2. Simplified diagram of voltage vectors with fluctuating dc-link voltage.

where δ is the delay phase between the sampled voltage and real-time voltage. From (13)–(16), the output voltage vector can be rewritten as

$$\begin{aligned} u_{so} &= u_{\rm sref}\cdot\frac{U_{\rm dc}+\Delta u_{\rm dc}\sin(2\omega_g t+\delta)}{U_{\rm dc}+\Delta u_{\rm dc}\sin(2\omega_g t)}\cdot e^{j\theta_r} \\ &= u_{\rm sref}\cdot\left(1+\frac{2\Delta u_{\rm dc}\sin(\delta/2)\cos(2\omega_g t+\delta/2)}{U_{\rm dc}+\Delta u_{\rm dc}\sin(2\omega_g t)}\right)\cdot e^{j\theta_r} \\ &= u_{\rm sref}\cdot(1+k_f\cos(2\omega_g t+\delta/2))\cdot e^{j\theta_r}. \end{aligned} \tag{17}$$

It can be seen that the output voltage vector is not exactly equal to the command voltage. Furthermore, there exists an alternating voltage component in the output voltage. Given that the dc component $U_{\rm dc}$ is far larger than $\Delta u_{\rm dc}$ and that $\delta/2$ is located in the range of $[-\frac{\pi}{2}\ \frac{\pi}{2}]$, (17) indicates that the magnitude of the ripple dc-link voltage and the delay phase are positive to the magnitude of the fluctuating voltage. Thus, the large magnitude of the ripple dc-link voltage can also lead to the voltage fluctuation. Based on (17), the output phase voltage can also be expressed as

$$\begin{aligned} u_{ao} &= u_{\rm sref}\cdot(1+k_r\cos(2\omega_g t+\delta/2))\cos(\omega_r t) \\ &= u_{\rm sref}\cdot\cos(\omega_r t) + u_{\rm sref}\cdot\frac{k_r}{2}\cos(2\omega_g t-\omega_r t+\delta/2) \\ &\quad + u_{\rm sref}\cdot\frac{k_r}{2}\cos(2\omega_g t+\omega_r t+\delta/2). \end{aligned} \tag{18}$$

From (18), the phase voltage contains harmonics with different frequencies. The frequency of $2\omega_g t-\omega_r$ has a more significant impact on the motor than the frequency of $2\omega_g t+\omega_r$ since the equivalent impedance is positive related to the frequency for the motor model [4]. Therefore, the beat phenomenon becomes severe when the operating frequency ω_r is close to the voltage ripple frequency ω_g. Based on (17), the output synchronous

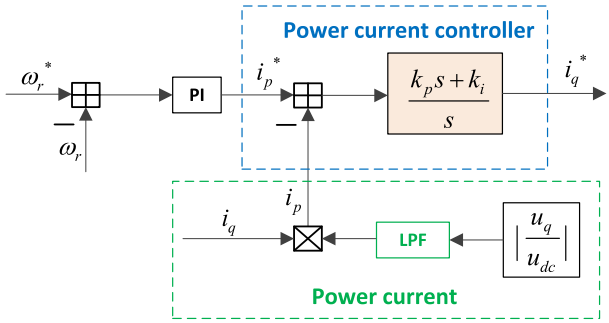

Fig. 3. Block diagram of the proposed power current controller.

voltage vector is induced as

$$u_{dq} = u_{\text{sref}} \cdot (1 + k_r \cos(2\omega_g t + \delta/2)) . \tag{19}$$

Here, the voltage in the synchronous frame contains a ripple component with constant frequency $2\omega_g$. This characteristic is helpful to suppress the ripple currents.

IV. Proposed Method

A. Principle and Implementation

A simplified diagram of power current control is shown in Fig. 3, including three components: a power current constructor, power current controller, and resonant controller. The power current is constructed as follows:

$$i_p = \left| \frac{u_q}{u_{\text{dc}}} \right| \cdot i_q \tag{20}$$

where u_q is the voltage command in the q-axis, i_q is the current in the q-axis, and i_p is the power current. Due to the ripple components of u_q and u_{dc}, an low-pass filter (LPF) is used to remove the ripple in u_q/u_{dc}. Hence, the power current can reflect the ripple information of current in the q-axis directly. To reveal the essence of the power current, the following equation is used:

$$u_q i_q = r_s i_q^2 + L_q \frac{di_q}{dt} i_q + i_q \omega_r (L_d i_d + \varphi_f) \tag{21}$$

where r_s is the stator resistance, L_d and L_q are the d-axis and q-axis inductances, respectively, ω_r is the rotor angular speed, and φ_f is the permanent flux. From (20) and (21), the power current has a nonlinear relationship with the current in the q-axis. The nonlinear equation can be simplified since the LPF can remove the term $L_q \frac{di_q}{dt} i_q$. Therefore, the open-loop transfer function of the power current is simplified approximately as

$$\frac{i_p}{i_q} = \left| \frac{R_s i_q + \omega_r (L_d i_d + \varphi_f)}{u_{\text{dc}}} \right| . \tag{22}$$

Furthermore, to guarantee the negative feedback in the power current control loop, the u_q/u_{dc} term should be positive. Thus, the absolute value is used instead of u_q/u_{dc}. From (22), controlling the target i_p to be constant brings a benefit to reject current ripple in the q-axis. As for the power current controller, the PI controller performs well. The detail parameter design and stability analysis are discussed in the next section.

B. Stability Analysis and Parameter Design

For a closed-loop system, the stability issue should be ensured in the first priority. In order to analyze the stability of the proposed method, the power current closed-loop diagram is given as Fig. 4, where e_q is the sum of the back electromotive force and coupling voltage, and $e^{-\tau s}$ is the transfer function of the time delay. The first part is the power current control loop. In this part, PI is used as the controller and the feedback variable is the constructed power current based on (22). The second part is the current control loop in synchronous frame. It contains a PI controller and a decoupling term considering back electromotive force. The third part is the transfer function of the time delay. The fourth part is the model of interior permanent magnet synchronous machine (IPMSM). The digital PWM and one-sampling-ahead requirement lead to a time delay of $\tau = 1.5Tsc$. For simplicity, this parameter can be ignored since this term can be compensated. Moreover, by using the classical zero-pole cancellation method, the parameters k_{ip} and k_{ii} are set as $k_{ip} = k_g L_q$ and $k_{ii} = k_g R_s$, where k_g is the bandwidth gain of the current loop. Therefore, the inner current closed-loop transfer function can be simplified as

$$\frac{i_q}{i_q^*} = \frac{k_g}{s + k_g}. \tag{23}$$

From (23), the inner current loop is equivalent to a time delay part. Ultimately, the power current closed-loop transfer function can be obtained

$$\frac{i_q}{i_p^*} = \frac{k_g(k_{pp}s + k_{pi})}{s^2 + (1 + k(u_{\text{dc}}, \omega_r)k_{pp})k_g s + k(u_{\text{dc}}, \omega_r)k_g k_{pi}} \tag{24}$$

where $k(u_{\text{dc}}, \omega_r) = \left| \frac{R_s i_q + \omega_r (L_d i_d + \varphi_f)}{u_{\text{dc}}} \right|$, and it is positive to the angular speed ω_r. Compared to the time constant of current, the change of speed is very slow. Thus, it can be treated as a constant parameter for steady state. Moreover, the gain is located in the range of $[0\ 1]$. As for the determination of bandwidth gain k_g, it is usually set as 1/8 to 1/10 of the switch frequency, which is set as 800. Thus, the parameters (k_{pp}, k_{pi}) determine the system stability and dynamic property. The system stability can be analyzed by means of the D-partition technique [27], [28]. In order to obtain the stable region, three steps are presented as follows.

Step 1: Using the equation $s = j\omega$ and (24), the closed-loop frequency characteristic function is obtained as

$$G(jw) = -\omega^2 + (1 + k(u_{\text{dc}}, \omega_r)k_{pp})k_g j\omega + k(u_{\text{dc}}, \omega_r)k_g k_{pi}. \tag{25}$$

Step 2: Set $G(jw) = 0$. Thus, both real and imaginary part terms are set as zero. According to the D-partition boundary theory, the parameters k_{pp} and k_{pi} can be expressed as

$$k_{pp} = \frac{-1}{k(u_{\text{dc}}, \omega_r)} \tag{26}$$

$$k_{pi} = \frac{\omega^2}{k(u_{\text{dc}}, \omega_r)k_g}. \tag{27}$$

Step 3: Obtain the stable region. The boundary of stable region is the curve of (k_{pp}, k_{pi}) when w changes from zero to infinity.

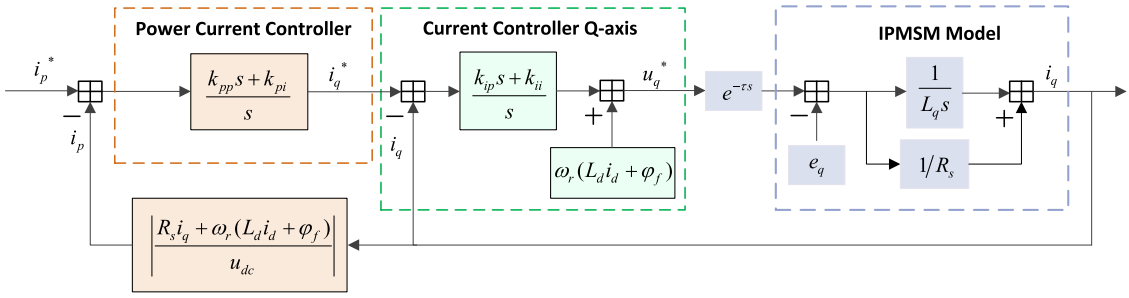

Fig. 4. Block diagram of the proposed power current closed-loop controller.

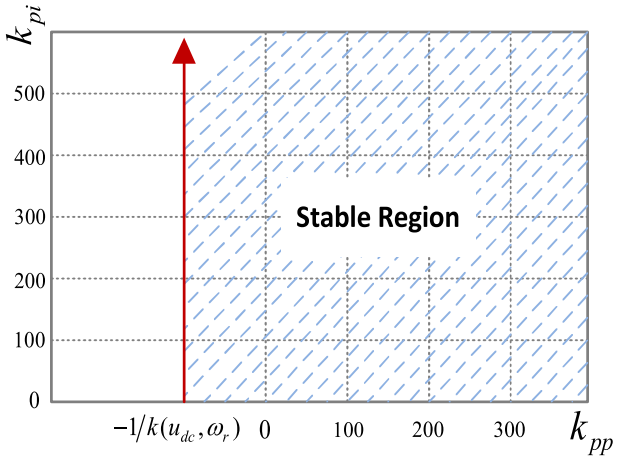

Fig. 5. Stable region with respect to parameters (k_{pp}, k_{pi}).

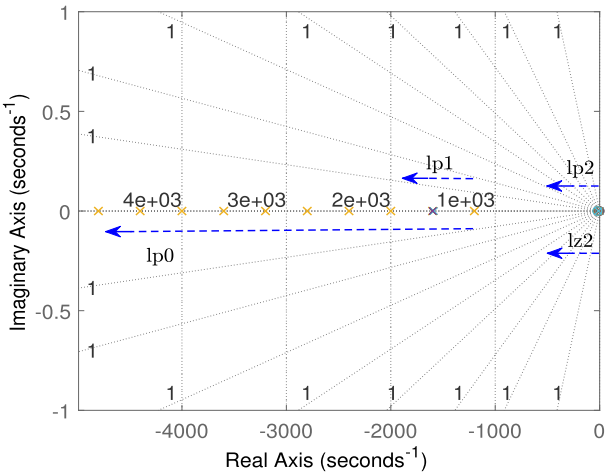

Fig. 6. Zero-pole map with respect to different values of (k_{pp}, k_{pi}).

In Fig. 5, the boundary curve is plotted. In order to make sure the system is stable, the value of (k_{pp}, k_{pi}) should be selected in the stable region. From (26) and (27), it can be observed that the parameters k_g and $k(u_{dc}, \omega_r)$ have an impact on the boundary of the stable region.

Although the parameters (k_{pp}, k_{pi}) are selected within the stable region, the values should be designed further to ensure the better steady state and dynamic performance. Usually, the root locus method is used to observe the trajectories of poles of closed-loop characteristic function. However, the closed-loop zero also has an important impact on the system dynamic response. Therefore, the pole-zero map is employed to find a suitable value of (k_{pp}, k_{pi}). The process of parameter design mainly contains following three steps.

Step 1: Set $k_{pi} = 0$. Thus, only one parameter k_{pp} exists. Accordingly, the closed-loop transfer function can be rewritten as

$$\frac{i_q}{i_p^*} = \frac{k_g k_{pp}}{s + (1 + k(u_{\rm dc}, \omega_r)k_{pp})k_g}. \tag{28}$$

As mentioned earlier, the gain $k(u_{\rm dc}, \omega_r)$ can be treated as a constant for a given speed. For simplicity to analyze the trajectories of the system poles, the gain, $0 \le k(u_{\rm dc}, \omega_r) \le 1$, is assumed to be 0.5. Then, the parameter k_{pp} is increased from zero to a limited value, such as $[1\ 2 \cdots 10]$. The pole trajectory is drawn as curve l_{p0}, as shown in Fig. 6. Similar to the conventional current loop design, the optimal value is selected as: $k_{pp} = 5$.

Step 2: Set $k_{pp} = 5$. The parameter k_{pi} is selected as $[1\ 5 \cdots 45]$. Accordingly, the zero-pole trajectories are drawn as curves l_{p1}, l_{p2}, and l_{z2}, respectively. From Fig. 7, there are two poles and one zero when the integral parameter k_{pi} is not equal to zero. Fig. 7(b) illustrates that the dominant pole is close to the imaginary axis, which will cause larger overshoot and deteriorate the transient performance. Generally, the zero affects the transient component. To attenuate the effect caused by the pole close to the imaginary axis, the zero should be close to the pole. Ultimately, the suitable parameter k_{pi} is set as 30.

C. Antidisturbance Analysis

As in the aforementioned analysis, there exists a voltage ripple in the output voltage due to the modulation error induced by the fluctuating dc-link voltage. The modulation error is one of the system disturbances $N(s)$. Therefore, the analysis of antidisturbance ability is necessary to validate the improvement of the proposed method.

From Fig. 4, the closed-loop transfer function of the conventional current loop for the disturbance is derived as

$$\frac{I_q(s)}{N(s)} = \frac{s}{L_q s^2 + (R_s + k_g L_q)s + k_g R_s}. \tag{29}$$

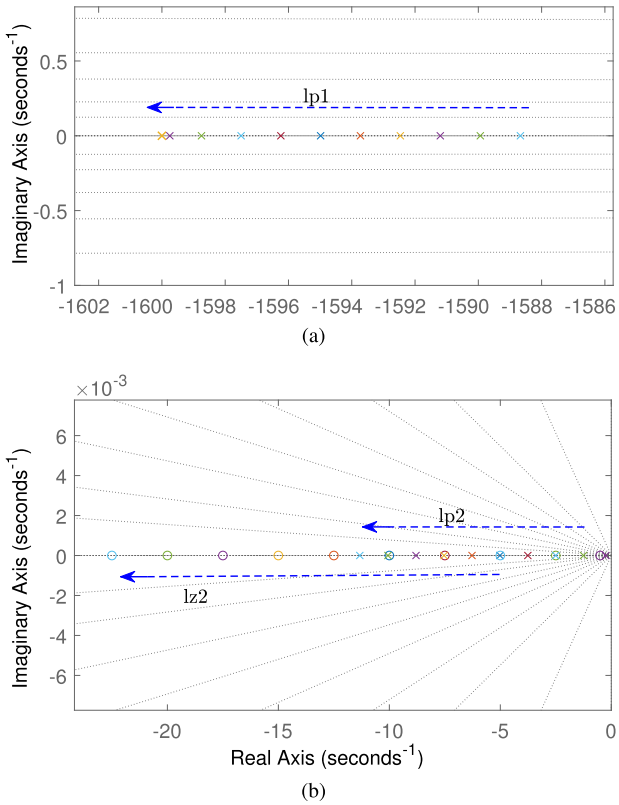

Fig. 7. Zoom in of the zero-pole map. (a) Pole trajectory of l_{p1}. (b) Zero-pole trajectories of l_{p2} and l_{z2}.

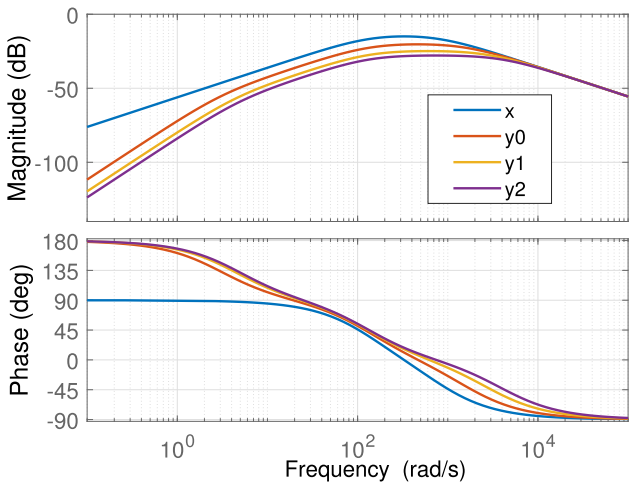

Fig. 8. Bode diagrams for the disturbance of conventional and proposed method, x: conventional method; y0: $k_{pp}=2$, $k_{pi}=12$; y1: $k_{pp}=5$, $k_{pi}=30$; and y2: $k_{pp}=8$, $k_{pi}=48$.

According to the transfer function (29), a Bode diagram is illustrated to show the antidisturbance ability, as shown in Fig. 8. For comparison, the closed-loop transfer function of the proposed power current loop for disturbance is also derived as

$$\frac{I_q(s)}{N(s)} = \frac{s^2}{a_3 s^3 + a_2 s^2 + a_1 s + a_0} \tag{30}$$

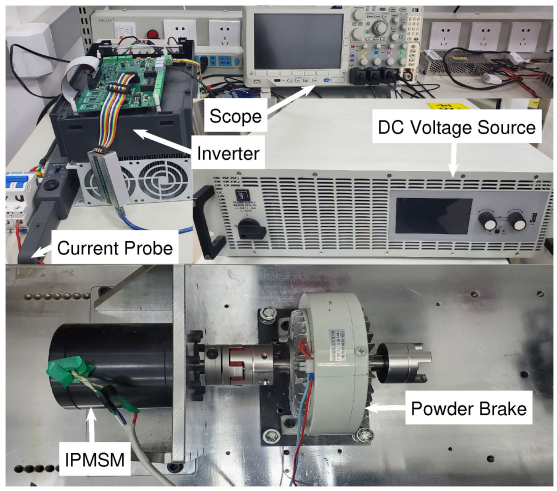

Fig. 9. Experimental platform, including a drive motor (2-kW IPMSM), powder brake, inverter, current probe, and scope.

TABLE I
MACHINE AND CONTROL PARAMETERS

Characteristics	Symbol	Values
Voltage ripple	Δu_{dc}	50 V
Rated power	P_N	2 kW
Rated frequency	f_N	180 Hz
Number of pole pairs	N_p	3
Stator resistance	R_s	0.85 Ω
d-aixs inductance	L_d	4 mH
q-aixs inductance	L_q	6 mH
Permanent flux	ψ_f	0.093 Wb

where $a_3 = L_q$, $a_2 = R_s + (1 + k(u_{\rm dc}, \omega_r)k_{pp})k_g L_q$, $a_1 = k_g(R_s(1 + k(u_{\rm dc}, \omega_r)k_{pp}) + L_q k(u_{\rm dc}, \omega_r)k_{pi})$, and $a_0 = k_g k(u_{\rm dc}, \omega_r)k_{pi}R_s$. Meanwhile, the control and machine parameters are set as $L_q = 6$ mH, $R_s = 0.8\Omega$, $k_{pp} = (2, 5, 8)$, and $k_{pi} = (12, 30, 48)$. According to the transfer function (30), the Bode diagrams are also illustrated in Fig. 8, where three sets of (k_{pp}, k_{pi}) are selected. From Fig. 8, the proposed method has a lower magnitude response for disturbance than the conventional method. The larger value of (k_{pp}, k_{pi}) results in better attenuation ability.

V. EXPERIMENTAL RESULTS

Several experiments are conducted to validate the performance of the proposed method. The experimental platform is shown in Fig. 9, where the encoder is not installed and the position senorless operation is implemented. The drive motor is a 2-kW IPMSM. Machine and control parameters are listed in Table I. The type of dsp is 32-b floating TMS320F28335. The sampling and PWM switching frequency is 6.25 kHz. The dc voltage source is EA-PSB-9750, which is fed to the inverter. As mentioned earlier, the magnitude of the ripple voltage is set as 50 V to induce enough ripple current. Also, the frequency of ripple voltage is set as 50 and 100 Hz. In order to remove the ripple component of the term $u_q/u_{\rm dc}$, the cutoff frequency of

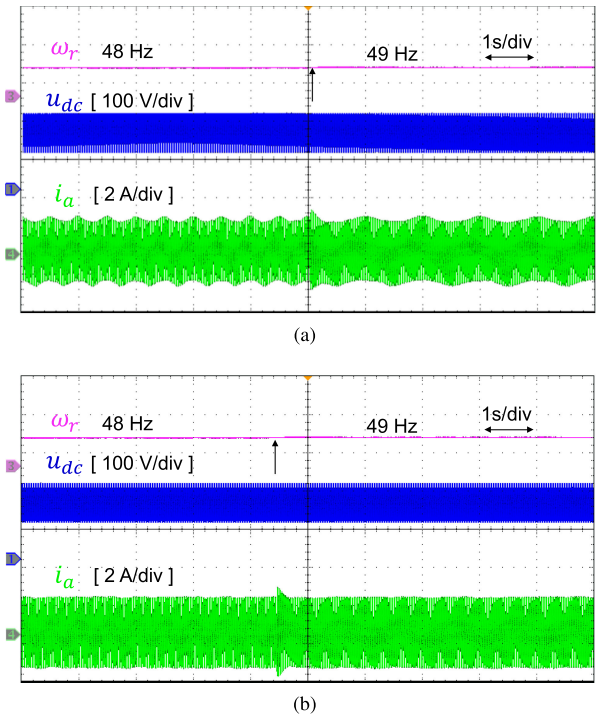

Fig. 10. Experimental waveforms with a dc-link ripple frequency of 50 Hz and no load. (a) Conventional method. (b) Proposed method.

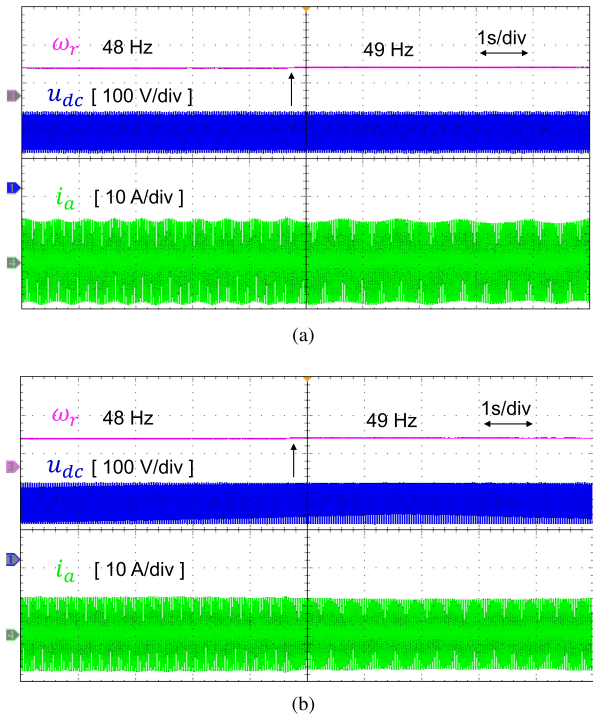

Fig. 11. Experimental waveforms with a dc-link ripple frequency of 50 Hz and full load. (a) Conventional method. (b) Proposed method.

LPF in Fig. 3 is set as 5 Hz. To evaluate the performance of current pulsation suppression, both the proposed PCC method and the conventional speed-current loop method are compared. For fairness, the parameters of current loop are the same and the bandwidth is set as 127 Hz.

Fig. 10 shows the system performance of both methods. From top to bottom, channel 3 is the rotor speed, channel 1 is the dc-link voltage, and channel 4 is the a-phase current. Fig. 10(a) shows the current control performance of conventional method. The ripple frequency of $u_{\rm dc}$ is set as 50 Hz. Accordingly, the speed changes from 48 to 49 Hz to show the low-frequency fluctuation of current. It can be observed that a ripple component appears in the phase current, which is called the beat phenomenon. As analyzed earlier, the beat frequency changes from 2 to 1 Hz when the speed changes from 48 to 49 Hz. By contrast, Fig. 10(b) shows the current control performance of the proposed method under the same experimental conditions. Obviously, the ripple current has been suppressed greatly. The full load experiment is tested, as shown in Fig. 11. A similar conclusion can be obtained. Figs. 12 and 13 are the zoom-in of Figs. 10 and 11, respectively. It is also noted that the waveforms of the proposed method are more sinusoidal. Thus, the proposed method can also suppress the current harmonics caused by the inverter nonlinearity and flux spatial harmonics.

Figs. 14 and 15 show the experimental results when the ripple frequency of $u_{\rm dc}$ is set as 100 Hz, where the speed changes from 98 to 99 Hz with no load and full load. Figs. 14(a) and 15(a) show the experimental waveforms of the conventional method with no load and full load, respectively. Figs. 14(b) and 15(b) show the experimental waveforms of the proposed method under the same conditions. As shown in Fig. 15, the current pulsations

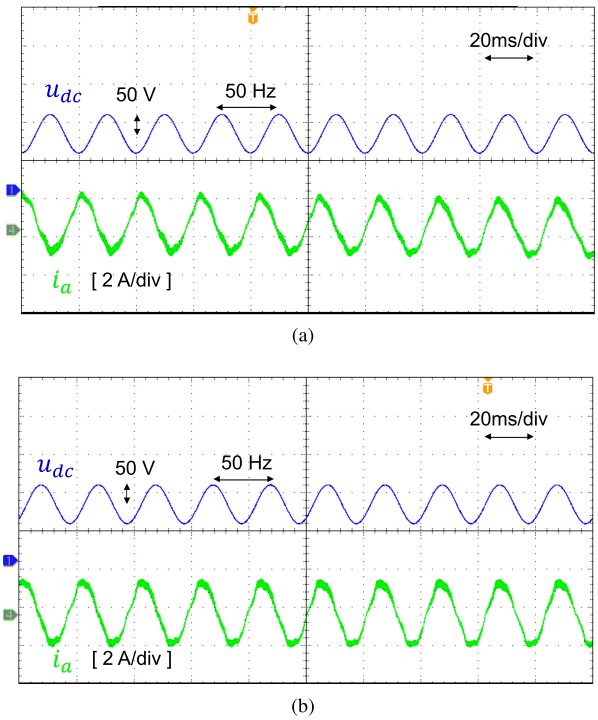

Fig. 12. Zoom-in of Fig. 10. (a) Conventional method. (b) Proposed method.

in q-axis have been reduced greatly before and after applying the proposed method. Accordingly, the torque pulsations have been reduced greatly from 17.86 to 5.36%. Before applying the proposed method, the phase current rms is fluctuated from 4 to 6 A. After applying the proposed method, the phase current

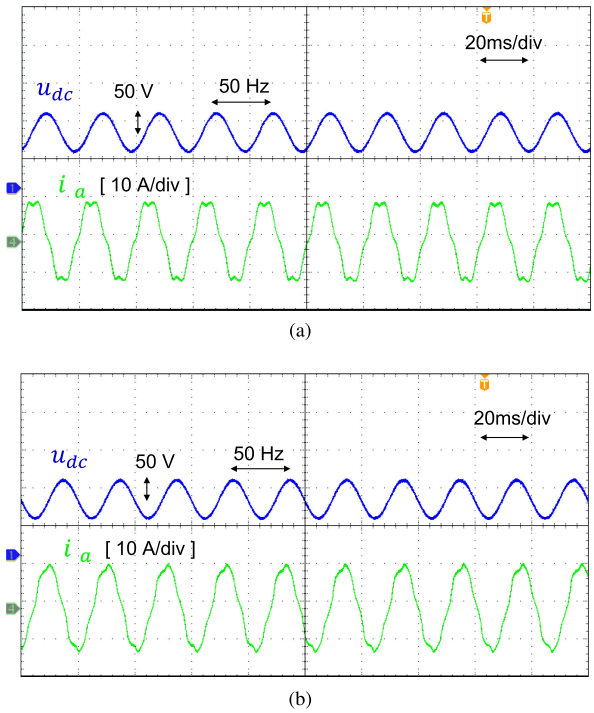

Fig. 13. Zoom-in of Fig. 11. (a) Conventional method. (b) Proposed method.

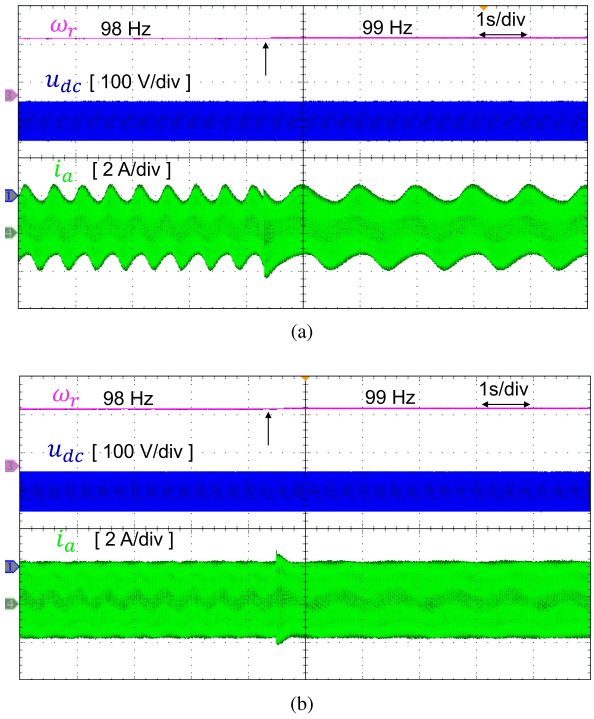

Fig. 14. Experimental waveforms with a dc-link ripple frequency of 100 Hz and no load. (a) Conventional method. (b) Proposed method.

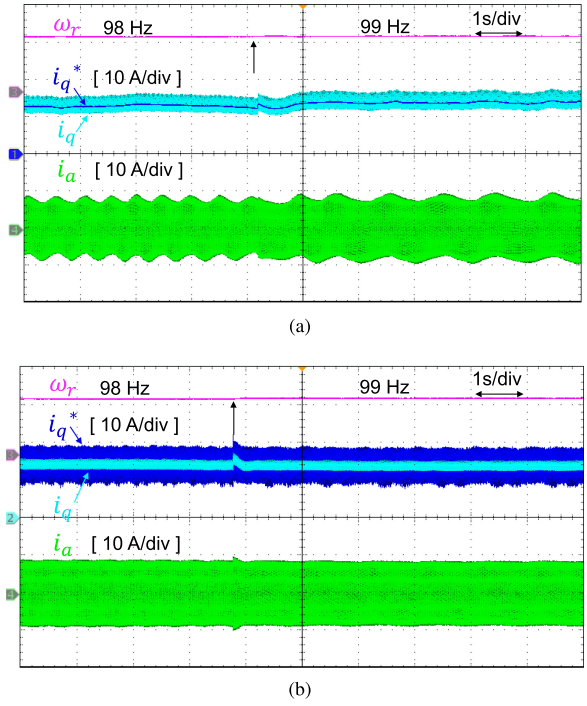

Fig. 15. Experimental waveforms with a dc-link ripple frequency of 100 Hz and full load. (a) Conventional method. (b) Proposed method.

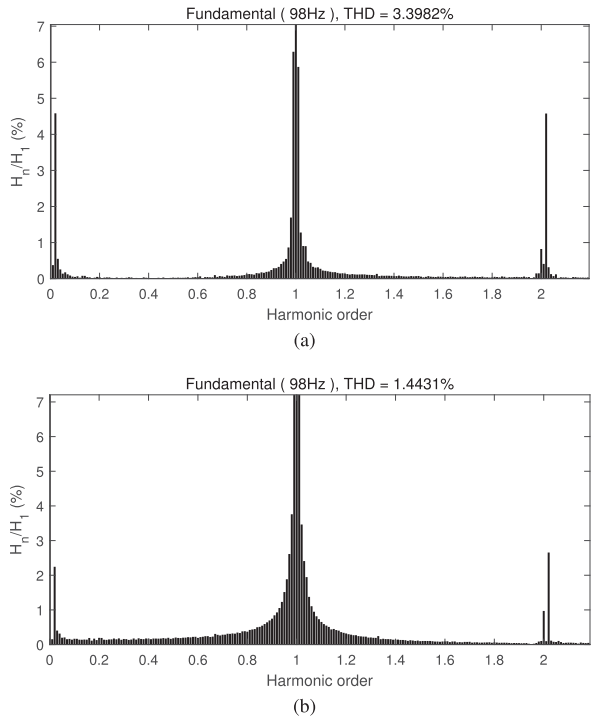

Fig. 16. Harmonics spectrum of one-phase current. (a) Proposed method disabled. (b) Proposed method enabled.

fluctuation is reduced to less than 1 A. The results are similar to those in Figs. 10 and 11.

The total harmonic distortion (THD) analysis when the operation speed is set as 98 Hz with full load is presented in Fig. 16. From the comparison between Fig. 16(a) and (b), the components at 2 and 198 Hz are reduced greatly when the proposed method is enabled. Also, the THD has been reduced from 3.3982 to 1.4431%.

The experimental results at rated speed 180 Hz with full load are shown in Fig. 17, where the proposed method is disabled in

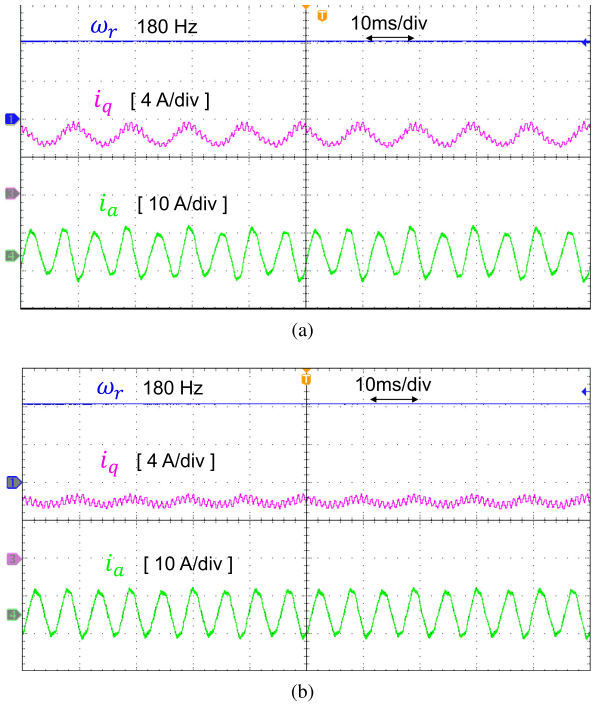

Fig. 17. Experimental waveforms at rated speed 180 Hz with full load. (a) Proposed method disabled. (b) Proposed method enabled.

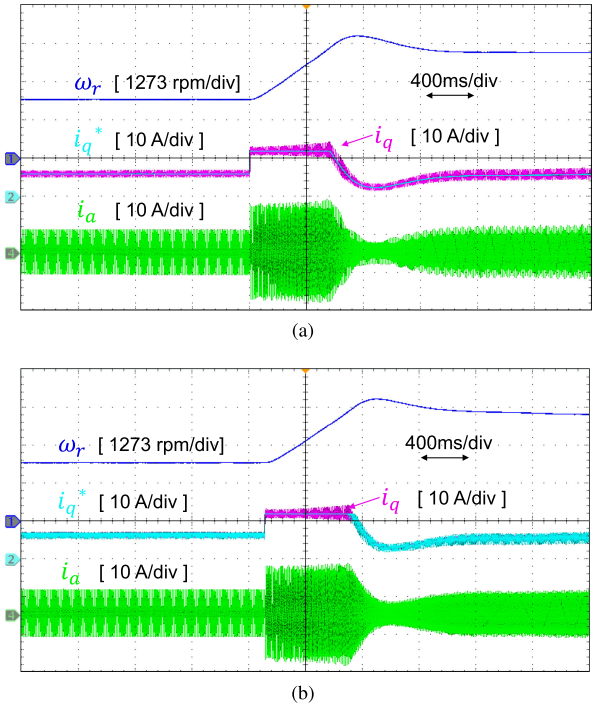

Fig. 18. Speed step from 100 to 180 Hz with full load. (a) Proposed method disabled. (b) Proposed method enabled.

Fig. 17(a) and enabled in Fig. 17(b). By the comparison, we can see that the low-frequency fluctuation in phase current has been suppressed greatly. Also, the ripple component of current in the q-axis at 100 Hz has been suppressed.

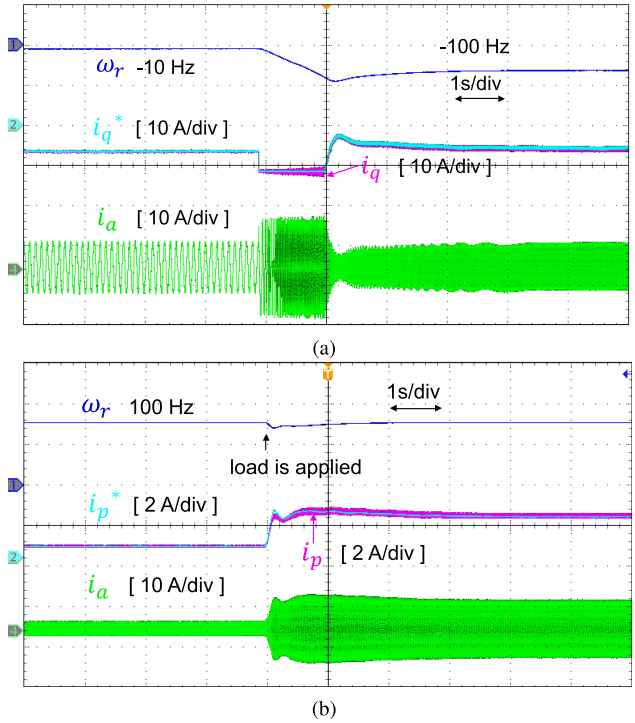

Fig. 19. Dynamic performance. (a) Speed step from −10 to −100 Hz. (b) External load step from 0 to 5 N · m.

Figs. 18 and 19 show the dynamic performances when the proposed method is enabled. It is seen that in Fig. 19(a), the proposed method works well when the speed runs from −10 to −100 Hz. In Fig. 19(b), the operation speed is set as 100 Hz and then the rated load is applied by a magnetic powder brake. The power current can track the command value accurately. The results confirm that the proposed has good dynamic performance.

VI. Conclusion

This article proposed a power current control method to suppress the low-frequency fluctuation in phase current. The power current is constructed and used as the control target. Accordingly, the power current loop is cascaded between the speed and current loops. Controlling the power current constant brings a benefit to reject the ripple of current. By the antidisturbance analysis, the proposed method has been proved the superiority of resisting the current disturbance, theoretically. The principle of parameter design is presented, and system stability is also analyzed by using the D-partition technique. Through sufficient experimental comparisons, the proposed control method exhibits better performance to suppress the disturbance component in current.

References

[1] K. Rajashekara, "Present status and future trends in electric vehicle propulsion technologies," *IEEE Trans. Emerg. Sel. Topics Power Electron.*, vol. 1, no. 1, pp. 3–10, Mar. 2013.

[2] Y. Zhang, J. Jin and L. Huang, "Model-free predictive current control of PMSM drives based on extended state observer Using Ultralocal Model," *IEEE Trans. Ind. Electron.*, vol. 68, no. 2, pp. 993–1003, Feb. 2021.

[3] Z. Salam and C. J. Goodman, "Compensation of fluctuating dc link voltage for traction inverter drive," in *Proc. 6th Int. Conf. Power Electron. Variable Speed Drives*, 1996, pp. 390–395.
[4] B. Gou, X.Feng, W. Song, K. Han, and X. Ge, "Analysis and compensation of beat phenomenon for railway traction drive system fed with fluctuating dc-link voltage," in *Proc. 7th Int. Power Electron. Motion Control Conf.*, 2012, pp. 654–659.
[5] J. Klima, M. Chomat, and L. Schreier, "Analytical closed-form investigation of PWM inverter induction motor drive performance under dc bus voltage pulsation," *IET Elect. Power Appl.*, vol. 2, no. 6, pp. 341–352, 2008.
[6] J. Lee and Y. Sun, "Adaptive harmonic control in PWM inverters with fluctuating input voltage," *IEEE Trans. Ind. Electron.*, vol. IE-33, no. 1, pp. 92–98, Feb. 1986.
[7] S. Zhao, X. Huang, Y. Fang, and J. Zhang, "Compensation of dc-link voltage fluctuation for railway traction PMSM in multiple low-switching-frequency synchronous space vector modulation modes," *IEEE Trans. Veh. Technol.*, vol. 67, no. 1, pp. 235–250, Jan. 2018.
[8] P. Dahler, G. Knapp, and A. Nold, "New generation of compact low voltage IGBT converter for traction applications," in *Proc. Eur. Conf. Power Electron. Appl.*, 2005, pp. 1–9.
[9] T. Larsson and S. Ostlund, "Active dc link filter for two frequency electric locomotives," in *Proc. Int. Conf. Elect. Railways United Europe*, 1995, pp. 97–100.
[10] N. Zhao, G. Wang, B. Li, R. Zhang, and D. Xu, "Beat phenomenon suppression for reduced dc-link capacitance IPMSM drives with fluctuated load torque," *IEEE Trans. Ind. Electron.*, vol. 66, no. 11, pp. 8334–8344, Nov. 2019.
[11] S. Zhao, X. Huang, Y. Fang, J. Zhang, and J. Wang, "DC-link-fluctuation-resistant control scheme for high power traction PMSM in six-step mode," in *Proc. 43rd Annu. Conf. IEEE Ind. Electron. Soc.*, 2017, pp. 2245–2251.
[12] S. Kouro, P. Lezana, M. Angulo, and J. Rodriguez, "Multicarrier PWM with dc-link ripple feedforward compensation for multilevel inverters," *IEEE Trans. Power Electron.*, vol. 23, no. 1, pp. 52–59, Jan. 2008.
[13] P. N. Enjeti and W. Shireen, "A new technique to reject dc-link voltage ripple for inverters operating on programmed PWM waveforms," *IEEE Trans. Power Electron.*, vol. 7, no. 1, pp. 171–180, Jan. 1992.
[14] S. Hadji, O. Touhami, and C. J. Goodman, "Vector-optimised harmonic elimination for single-phase pulse-width modulation inverters/converters," *IET Elect. Power Appl.*, vol. 1, no. 3, pp. 423–432, 2007.
[15] H. Ouyang, K. Zhang, P. Zhang, Y. Kang, and J. Xiong, "Repetitive compensation of fluctuating dc link voltage for railway traction drives," *IEEE Trans. Power Electron.*, vol. 26, no. 8, pp. 2160–2171, Aug. 2011.
[16] S. Funabiki and Y. Sawada, "A computative decision of pulse width in three-phase PWM inverter," in *Proc. Conf. Rec. IEEE Ind. Appl. Soc. Annu. Meeting*, 1988, pp. 694–699.
[17] S. Zhao, X. Huang, Y. Fang, and H. Zhang, "DC-link-fluctuation-resistant predictive torque control for railway traction permanent magnet synchronous motor in the six-step operation," *IEEE Trans. Power Electron.*, vol. 35, no. 10, pp. 10982–10993, Oct. 2020.
[18] X. H. Wu, S. K. Panda, and J. X. Xu, "DC link voltage and supply-side current harmonicsminimization of three phase PWM boostrectifiers using frequency domain basedrepetitive current controllers," *IEEE Trans. Power Electron.*, vol. 23, no. 4, pp. 1987–1997, Jul. 2008.
[19] H. Jung, S. Chee, S. Sul, Y. Park, H. Park, and W. Kim, "Control of three-phase inverter for ac motor drive with small dc-link capacitor fed by single-phase ac source," *IEEE Trans. Ind. Appl.*, vol. 50, no. 2, pp. 1074–1081, Mar./Apr. 2014.
[20] K. Lee *et al.*, "Closed-form analysis of adjustable-speed drive performance under input-voltage unbalance and sag conditions," *IEEE Trans. Ind. Appl.*, vol. 42, no. 3, pp. 733–741, May/Jun. 2006.
[21] L. J. Diao, K. Dong, S. B. Yin, J. Tang, and J. Chen, "Ripple analysis and control of electric multiple unit traction drives under a fluctuating dc link voltage," *J. Power Electron.*, vol. 16, no. 5, pp. 1851–1860, 2016.
[22] Y. Lei, K. Wang, L. Zhao, and Q. Ge, "An improved beatless control method of ac drives for railway traction converters," in *Proc. 19th Int. Conf. Elect. Mach. Syst.*, 2016, pp. 1–5.
[23] M. E. De Oliveira Filho, E. R. Filho, K. E. B. Quindere, and J. R. Gazoli, "A simple current control for matrix converter," in *Proc. Conf. Rec. IEEE Ind. Appl. Conf. 41st IAS Annu. Meeting*, 2006, pp. 2090–2094.
[24] M. E. D. O. Filho, J. R. Gazoli, A. J. S. Filho, and E. R. Filho, "A control method for voltage source inverter without dc link capacitor," in *Proc. Power Electron. Specialists Conf.*, 2008, pp. 4432–4437.
[25] W. Shi, F. Lin, and Z. Yang, "A new method based on PIR controller to reject torque and current ripple under fluctuating dc voltage for high-speed train traction drives," in *Proc. Int. Conf. Elect. Mach. Syst.*, 2013, pp. 1–5.
[26] Y. Lei, K. Wang, L. Zhao, Q. Ge, Z. Li, and Y. Li, "An improved torque and current pulsation suppression method for railway traction drives under fluctuating dc-link voltage," *IEEE Trans. Power Electron.*, vol. 33, no. 10, pp. 8565–8577, Oct. 2018.
[27] X. Zhang, H. Li, S. Yang, and M. Ma, "Improved initial rotor position estimation for PMSM drives based on HF pulsating voltage signal injection," *IEEE Trans. Ind. Electron.*, vol. 65, no. 6, pp. 4702–4713, Jun. 2018.
[28] C. Hwang, L. F. Hwang, and J. H. Hwang, "Robust D-partition," *J. Chin. Inst. Engineers*, vol. 33, no. 6, pp. 811–821, 2010.

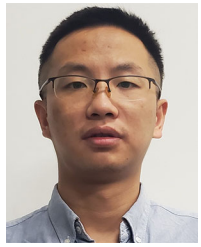

Jiali Liu was born in Anhui, China, in 1989. He received the B.S. degree in electrical engineering from the North China Institute of Science and Technology, Hebei, China, in 2013, and the M.S. degree in electrical engineering in 2017 from the North China University of Technology, Beijing, China, where he is currently working toward the Ph.D. degree in electrical engineering.

His current research interests include predictive control of permanent-magnet motor drives.

Yongchang Zhang (Senior Member, IEEE) received the B.S. degree from Chongqing University, Chongqing, China, in 2004, and the Ph.D. degree from Tsinghua University, Beijing, China, in 2009, both in electrical engineering.

From August 2009 to August 2011, he was a Postdoctoral Fellow with the University of Technology Sydney, Ultimo, NSW, Australia. He joined the North China University of Technology, Beijing, in August 2011, as an Associate Professor, where he is currently a Full Professor. He has authored or coauthored more than 100 technical papers in the area of motor drives, pulsewidth modulation, and ac/dc converters. His current research interests include model predictive control for power converters and motor drives.

Dr. Zhang is a Fellow of the Institute of Engineering and Technology. He serves as the Associate/Guest Editor for several international journals, such as the IEEE JOURNAL OF EMERGING AND SELECTED TOPICS IN POWER ELECTRONICS. He is the Technical Program Co-Chair of 5th/6th IEEE International Conference on Predictive Control of Electrical Drives and Power Electronics.